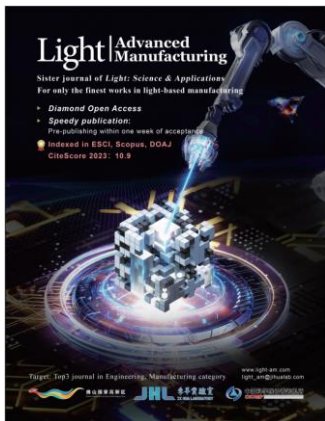**Accepted Article Preview: Published ahead of advance online publication**

High-speed complex field modulation using binary phase-engraved superpixels

Patrick Kilcullen, Jingdan Liu, Youmin Wang, Lei Gong, Jinyang Liang

Main Text

High-speed complex field modulation using binary phase-engraved superpixels

Patrick Kilcullen[1], Jingdan Liu[1,†], Youmin Wang[2], Lei Gong[3], Jinyang Liang[1,*]

[1]Laboratory of Applied Computational Imaging, Centre Énergie Matériaux Télécommunications, Institut National de la Recherche Scientifique, Universitéu Québec, 1650 boulevard Lionel-Boulet, Varennes, Québec J3X1P7, CANADA

[2]Reality Laboratory, Meta Platforms, 9845 Willows Road, Redmond, Washington 98052, USA

[3]Department of Optics and Optical Engineering, University of Science and Technology of China, 96 JinZhai Road, Hefei, Anhui 230026, CHINA

[†]Current address: Shanghai Institute of Optics and Fine Mechanics, Chinese Academy of Sciences, Shanghai 201800, CHINA

*Corresponding author: jinyang.liang@inrs.ca

ABSTRACT

Complex field modulation (CFM) has found a plethora of applications in physics, biomedicine, and instrumentation. Among existing methods, superpixel-based CFM has been increasingly featured because of its advantages in high modulation accuracy and its compatibility with high-speed spatial light modulators (SLMs). Nonetheless, the mainstream approach based on binary-amplitude modulation confronts limitations in optical efficiency and dynamic range. To surmount these challenges, we develop binary phase-engraved (BiPE) superpixel-based CFM and implement it using the phase light modulator (PLM)—a new micro-electromechanical system-based SLM undergoing development by Texas Instruments in recent years. Using BiPE superpixels, we demonstrate high-accuracy spatial amplitude and phase modulation at up to 1.44 kHz. To showcase its broad utility, we apply BiPE superpixel-based CFM to beam shaping, high-speed projection, and augmented-reality display.

INTRODUCTION

Full modulation of complex optical fields (i.e., amplitude and phase) has found widespread applications including optical communication[1,2], three-dimensional display[3,4], biomedical imaging[5,6], and astronomy[7,8]. Among dazzling progress in the past decade, high accuracy, high speed, and versatility have been increasingly featured as important technical specifications to

evaluate the overall capability of optical instruments for complex field modulation. In turn, improved specifications have contributed to new applications. For example, high-precision laser beam shaping produces homogeneous optical lattices for ultracold atoms[9] and generates uniform optical undulators for free-electron lasers[10]. For biomedical imaging, adaptive wavefront engineering allows biological dynamics to be observed in deep tissue[11–13]. In augmented reality (AR) and virtual reality (VR) displays, high-speed image projection improves users' experience by reducing image latency with eye movement[14]. For the manufacturing of planar optics, photopatterned liquid crystals (LCs) have been used to generate optical vortex beams with high topological charge[15,16].

Spatial light modulators (SLMs) play a key role in the overall performance of complex field modulation (CFM). These advanced optoelectronic devices consist of a two-dimensional (2D) array of electronically addressable pixels whose optical properties (e.g., effective birefringence and reflection direction) can be independently controlled to modulate incident light's amplitude and phase. To date, the most popularly used SLMs for CFM have been liquid crystal on silicon (LCOS) devices[17]. LCOS-based SLMs use a liquid crystal layer on a silicon chip with an array of reflective electrodes. By exploiting birefringence in electro-optical liquid crystals, the phase can be modified by adjusting the bias across a liquid crystal cell. However, the refresh rate of state-of-the-art LCOS-based SLMs is limited to sub-kHz due to the viscoelasticity of liquid crystal materials[18].

To overcome limitations in speed, SLMs based on micro-electromechanical systems (MEMSs) can be used with affordability. In this category, deformable mirrors (DMs) are a popular choice. These devices combine a reflective membrane with a number of underlying control mechanisms such as electrostatic or piezoelectric actuators. Operating as individual points of displacement control, actuators may serve to deform a continuous membrane surface or to contribute multi-axis control to individual mirror segments[19]. While the speed of such actuation is capable of reaching the 10-kHz range, the complexity of DM architectures limits their degree of miniaturization, leading them to suffer from low actuator counts on the order of several thousand per chip[20,21]. The limitation of pixel numbers for MEMS-based SLMs however is lifted by digital micromirror devices (DMDs), which have megapixel frame sizes and tens-of-kHz-level pattern refresh rates[22]. Each micromirror, suspended on micron-scale flexure hinges, can be tilted at two angles that either reflect or deflect light along the optical path. Complex fields can be encoded in

a single binary hologram[23–25], which possesses practical advantages in terms of speed, device calibration, and efficient data storage. Nonetheless, the binary amplitude modulation cannot diffract the majority of energy to the desired diffraction order[26], which significantly limits the overall efficiency to <10%.

An attractive candidate to solve the aforementioned problems is the phase light modulator (PLM) undergoing development by Texas Instruments[27–29]. The PLM has incorporated all of the core manufacturing technologies used for DMD fabrication into the constraints of its design, including pixel structure, base-layer CMOS drive circuitry, materials processing, and chip packaging[27]. Thus, the PLM is largely compatible with existing DMD drivers and control modules and shares similar advantages including high stability and long endurance[29]. Moreover, whereas a "tip-tilt" actuation design latches the DMD's micromirrors to two angles, the PLM's micromirrors actuate via "piston-mode" displacements electrostatically driven by a 2×2 CMOS memory cell footprint that enables access to 16 positional states. The MEMS-based architecture endows the PLM with many promising advantages over the LCOS devices and deformable mirrors, including high mirror counts, kHz-level pattern refresh rates, immunity to pixel crosstalk, polarization independency, and high operation stability[27].

Despite these advantages, existing PLMs do not have a uniform distribution of accessible phase levels[30,31]. Although stemming from the limitations of existing fabrication processes rather than their MEMS architecture[29], this drawback reduces the information carried by the pixels to below 4 bits in practice. More importantly, this phase-distribution characteristic could require some applications to rely on device-specific calibration and compensation—a situation in contrast to the reliable interchangeability of DMDs that do not exhibit intermediate states between "ON" and "OFF". This analysis suggests that the use of binary phase to avoid the need to compensate for non-uniformities in current PLM devices could be an effective strategy for their utilization in sensitive applications.

In this work, we develop CFM at the kHz level using binary phase-engraved (BiPE) superpixels based on the PLM platform. Compared to existing superpixel-based CFM based on binary amplitude SLMs, BiPE superpixel-based CFM increases optical efficiency and enables a more than one order of magnitude improvement in the number of possible complex field values. We demonstrate BiPE-superpixel-based CFM for beam shaping, high-speed holographic display, and see-through AR.

METHODS

System

The experimental setup of CFM using BiPE superpixels is schematically depicted in Fig. 1a. Light from a continuous-wave laser (λ=532 nm, M Squared Equinox), reflected by a beamsplitter (BS1), illuminates a PLM (Texas Instruments DLP6750Q1EVM) at normal incidence. The PLM consists of a 1358×800 ($W \times H$) array of piston-actuated reflective square micromirrors of pitch $d = 10.8$ μm with a pattern refresh rate of 1.44 kHz. The binary phase pattern loaded on the PLM is imaged to a CCD camera (Optronis CP70-1HS-M-1900) by a 4-f system formed by lenses L1 and L2 (both with a focal length of $f = 150$ mm) together with a circular iris (Thorlabs ID20) narrowed to a diameter of ~1 mm. L1 is mounted on a 2D translation stage to provide a lateral shift relative to the spatial filter. Besides the 4-f imaging system, a secondary reference beam path is present for interferometric measurements. The light transmitted through BS1 is reflected by two mirrors M1 and M2. A second beamsplitter (BS2) placed after L2 allowed for the PLM-modulated field and the reference beam to form an interference pattern at the camera. Details of the PLM and the alignment procedure of this system are provided in Supplementary Notes 1 and 2 and Supplementary Fig. S1.

Operating principle

The operation of BiPE-superpixel-based CFM can be illustrated by the case of a one-dimensional superpixel consisting of four pixels shown in Fig. 1b. Due to the lateral offset of the first lens, light that passes through the spatial filter carries a tilted phase amounting to a phase pre-factor of $e^{i\Delta\phi}$ across the width of the superpixel. If the field influences of the PLM pixels are written as complex phasors U_k for $k = 0, \dots, 3$, then the low-pass filtering induced by the 4-f system blurs the image of the superpixel at the imaging plane, leading to the complex field being determined by the sum of the individual PLM pixel phasors multiplied by the appropriate phase pre-factors induced by the tilted wavefront.

Using this configuration, the array of PLM pixels is divided into superpixel blocks of size $n \times n$, each of which is dedicated to the complex control of the optical field at a conjugate point at the target plane. The choice of n then determines the related parameters of spatial filtering and the offset of the first lens, visualized in Fig. 1c. The diameter of the circular spatial filter is chosen

such that the spatial frequencies passed at the Fourier plane restrict the spatial resolution to above the size of a superpixel. As a result, the field contributions of individual pixels, each with a point spread function determined by the spatial filter size, synthesize the desired complex field at the target plane via the superposition of their contributions. In particular, choosing the period of the maximum spatial frequency equal to a number ρ of superpixels at the PLM plane requires the use of a spatial filter of opening radius $r = \frac{\lambda f}{\rho n d}$. By setting a lower bound value of $\rho = 2$, an appropriate balance between field accuracy and spatial resolution can be afforded for various sizes of n [Ref. 25].

Compared to superpixel-based CFM using binary amplitude modulation, the binary phase set by the individual PLM pixels allows for the phase gradient seen across a superpixel to be reduced, while still preserving the ability of individual pixels to uniformly access the full range of possible field phases. An exemplary phase gradient profile is depicted in Fig. 1d, in which a range of phase pre-factors of only $[0, \pi]$ radians is needed within a superpixel to provide a full 2π radians of phase modulation. These phase gradients, expressed as $\Delta\phi_x^{\mathrm{PLM}} = \frac{\pi}{n^2}$ and $\Delta\phi_y^{\mathrm{PLM}} = \frac{\pi}{n}$ in units of radians per PLM pixel, thus corresponding to a spatial filter position of $\frac{\lambda f}{2d}\left(\frac{-1}{n^2}, \frac{-1}{n}\right)$ at the Fourier plane. As this position is closer to that of the zeroth diffraction order behind L1, BiPE-superpixel-based CFM is more efficient compared to the counterpart based on binary amplitude superpixels (see derivation and comparison in Supplementary Note 3, Supplementary Table S1, and Supplementary Fig. S2).

BiPE-superpixel-based CFM also benefits in terms of light efficiency and the granularity of the field phasors addressable by the superpixel states. The states of PLM pixels in a superpixel can be specified by using a configuration vector $\boldsymbol{c}$ of n^2 elements with $c_k \in \{0,1\}$ and $k = 0, \cdots, n^2 - 1$ according to row-major ordering. Taking the configuration values $c_k = 0$ and $c_k = 1$ as representing PLM-induced phase shifts of 0 and π radians respectively, and assuming uniform illumination, the corresponding output field of a PLM superpixel is proportional to

$$U_{\mathrm{PLM}}(\boldsymbol{c}) = \sum_{k=0}^{n^2-1} \exp\left[i\pi\left(\frac{k}{n^2} + c_k\right)\right] \tag{1}$$

A "gamut" plot of $U_{\mathrm{PLM}}(\boldsymbol{c})$ ranging over the set of all 2^{n^2} possible configuration vectors in the complex plane with $n = 4$ is shown in Fig. 2a, with the particular phasor and superpixel configurations corresponding to two selected gamut elements shown in Fig. 2b and Fig. 2c, and

Fig. 2d and Fig. 2e, respectively. In this case, equation (1) represents a one-to-one mapping that produces a maximally sized gamut consisting of $2^{n^2} = 65,536$ distinct output phasors with a maximum magnitude of $R_{\text{PLM}} = 10.20$. Compared to superpixels based on binary amplitude modulation, BiPE superpixels do not discard any component of their incident illumination, which leads to salient advantages in achievable gamut size and cardinality. Full details of the comparison between the gamut sets produced by these two methods are provided in Supplementary Note 4 and Supplementary Fig. S3.

Creation of PLM control images

The PLM is partitioned into groups of superpixels arranged as an array of width $\widetilde{W} = \left\lfloor \frac{W}{n} \right\rfloor$ and height $\widetilde{H} = \left\lfloor \frac{H}{n} \right\rfloor$. To generate a desired complex field $\tilde{T}(u,v)$ of discrete coordinates $u = 0, \ldots, \widetilde{W} - 1$ and $v = 0, \ldots, \widetilde{H} - 1$ with a normalized amplitude profile (i.e., $|\tilde{T}(u,v)| \leq 1$), the corresponding superpixel images can be created by selecting configuration vectors $C(u,v)$ that minimize the difference between the target field and corresponding field output found in the superpixel gamut, i.e.,

$$C(u,v) = \arg \min_{c} \left| U_{\text{PLM}}(\boldsymbol{c}) - R \exp\left[-i\pi \left(\frac{1}{n}u + v \right) \right] \tilde{T}(u,v) \right|^2 \tag{2}$$

where R is a constant parameter ($R \leq R_{\text{PLM}}$) specifying the maximum field amplitude possible for a given n in the superpixel gamut, the term $\exp\left[-i\pi \left(\frac{1}{n}u + v \right) \right]$ compensates for starting offsets in the overall phase gradient seen by the superpixels, and the $\arg \min_{c}(\cdot)$ operator returns the value of $\boldsymbol{c}$ that minimizes its argument function. The information specified by equation (2), consisting of an $\widetilde{W} \times \widetilde{H}$ array of n^2-bit configuration vectors, is then converted into an $W \times H$ binary image suitable for direct display on the PLM via the reshaping of the vectors $C(u,v)$ into $n \times n$ blocks utilizing row-major ordering, followed by the 2D concatenation of all such blocks within the superpixel array. Details of these conversion steps are provided in Supplementary Note 5.

RESULTS

System configuration

Complex field modulation was carried out using superpixels of size $n \times n = 4{\times}4$, corresponding to a target plane resolution of $\widetilde{W} \times \widetilde{H} = 339{\times}200$ superpixels. To increase the space of available phase values for superpixels controlling points of maximum target field amplitude, the range of accessible PLM gamut points was restricted through the choice of $R = 0.8R_{\mathrm{PLM}}$ in equation (2), thus concentrating the range of PLM modulation to the gamut regions of the highest density in the complex plane. The measurement of complex fields was carried out using camera imagery of interference patterns captured synchronously with the PLM framerate of 1.44 kHz. Full details of the design of PLM control patterns supporting background field compensation and the corresponding analysis of camera image data are provided in Supplementary Note 6.

Demonstration of amplitude and phase control

To demonstrate the independent control of target field amplitude and phase, we tested the display of an amplitude-only pattern and a phase-only pattern with bi-directional linear ramps. For the display of the amplitude-only field shown in Fig. 3a, the ramp sections have a horizontal extent of 250 superpixels that cover the range of $[0,1]$ with the background region set to 0.5. The reconstructions of the target field amplitude show successful amplitude modulation across the full range of gamut intensities with the background phase held constant. It is noted that the accuracy of the deployed phase measurements was disrupted for regions of the target plane with near-zero amplitude due to the finite dynamic range of the camera's CCD sensor. The averaged profiles of the linear ramp regions show good agreement with the ground truth (Fig. 3b), corresponding to a root-mean-squared error (RMSE) value of 0.115 computed from the magnitude of the complex error between the measured and ground-truth fields.

For the display of the phase-only field shown in Fig. 3c, the mirrored ramp sections also have a width of 250 superpixels but cover the range of $[-\pi, \pi]$ with a background region value of 0 radians. The pattern has a uniform normalized amplitude value of 1.0. The bottom panel in Fig. 3c shows the high-quality reconstruction of the phase distribution. As shown in Fig. 3d, the averaged profile of the measured phase ramp shows good conformity compared with the ground truth, corresponding to an RMSE value of 0.183.

Demonstration of complex optical fields

To demonstrate potential applications of BiPE-superpixel-based CFM in laser beam shaping, we generated single-mode target fields of a Bessel beam[32] and a Laguerre-Gaussian (LG) beam[33]. Noted for several attractive properties of its wave propagation behavior, the Bessel beam has received wide interest in numerous applications ranging from biomedical imaging in ophthalmology[34] to photoacoustic microscopy[14] and electron microscopy[35]. As a family of exact solutions to the Helmholtz equation governing scalar wave propagation, Bessel modes are characterized by an integer n_{BB} characterizing the beam order and in general feature intensity profiles consisting of rings of circular fringes. For this demonstration, we selected the first Bessel mode of zero order for which the normalized field intensity at the center of the beam's depth of field can be expressed as

$$\tilde{T}_{BB}(r, \varphi) = J_0(k_r r) \tag{3}$$

where (r, φ) specify the polar pixel coordinates of a point relative to the center of the PLM on the optical axis, $k_r = 0.15$ is a parameter chosen to express the radial length scale, and $J_0(x)$ is the zeroth-order Bessel function of the first kind. The amplitude and phase profiles of the ground truth Bessel beam are shown as the left images in Fig. 4a and 4b, respectively. The results generated by BiPE superpixel-based CFM are shown as the right images. The averaged profile of the measured amplitude from a center-crossing rectangular region is plotted in Fig. 4c. These results illustrate a high degree of fidelity (with an RMSE value of 0.145) to the prescribed field amplitude as well as the phase inversions imposed by the negative-going oscillations of the Bessel function.

The intensity profiles of LG modes are defined by the product of a Gaussian and an associated Laguerre polynomial, which accepts two non-negative integer parameters l and p that control the appearance of concentric intensity rings, as well as a net azimuthal phase change. In this experiment, we chose $l = 1$ and $p = 0$ to generate a "donut" beam that is central to applications in optical tweezers and microscopy[36–39]. In this case, the optical field is given by

$$\tilde{T}_{LG}(r, \varphi) = A r \exp\left[i\left(\varphi - \frac{r^2}{w^2}\right)\right], \tag{4}$$

where A is a positive scalar that normalizes the maximum field amplitude, and $w = 30$ is a parameter chosen to define the radial length scale. The amplitude and phase profile of the ground truth donut beam are shown as the left images in Fig. 4d and 4e and the corresponding results generated by BiPE-superpixel-based CFM are shown as the right images (with an RMSE value of 0.101). The averaged amplitude and phase profiles (Fig. 4f and 4g) show that the PLM-induced

field successfully mirrors that of the LG beam, including the point of minimum intensity at the beam center and the phase change along the azimuthal direction.

Application to advanced display

To demonstrate BiPE-superpixel-based CFM for advanced display applications, we displayed 24-frame animated sequences containing both amplitude and phase content at various speeds. First, Fig. 5a and Fig. 5b show exemplary results of amplitude-only and phase-only digits at the maximum display rate of the PLM device of 1.44 kHz. To support the characterization of complex fields at full device speed, amplitude and phase information was extracted from single CCD fringe images recorded synchronously with the display of each frame. Full details of the procedure used for single-shot amplitude and phase recovery are also provided in Supplementary Note 6. Using a multi-frame procedure for greater precision, we also displayed and characterized complex fields at 60 Hz, as shown in Fig 5c. Animated movies of these datasets are provided as Supplementary Movies 1 and 2.

Finally, to demonstrate the suitability of BiPE-superpixel-based CFM for AR display, we replaced the reference arm with an imaging path that combined PLM-generated light fields with a view of a real scene on the camera sensor. The setup, illustrated in Fig 6a, consisted of a real scene imaged to the camera sensor via BS2 by a 50 mm camera lens (Nikon AF f/1.8D) and relay lens (L3, f = 150 mm, Thorlabs AC508-150-A-ML). Two scenes are depicted in Fig. 6b and Fig. 6c, both composed of two toy figurines from the "Star Wars" franchise. The PLM displayed animations (implemented as amplitude-only fields) that emulated the ignition of two lightsabers and the reflection of a laser pulse by a lightsaber. Selected frames from the animated AR display sequence are shown in Fig. 6d and Fig. 6e. Animated movies of the captured datasets of both scenes are provided as Supplementary Movies 3 and 4. Details of the measurement of calibration information and the creation of the animated sequence are provided in Supplementary Note 7 and Supplementary Fig. S4.

DISCUSSION

We have developed BiPE-superpixel-based CFM and implemented it using the PLM—a new MEMS-based SLM undergoing development by Texas Instruments. When combined with current PLM prototypes, BiPE superpixels circumvent the PLM's drawback of nonlinear phase response,

while also achieving high-accuracy spatial amplitude and phase modulation at speeds of up to 1.44 kHz. BiPE-superpixel-based CFM has been used for several applications, such as structured beam shaping, advanced image projection, and AR display.

BiPE-superpixel-based CFM holds three key advantages over superpixel-based CFM achieved with binary amplitude modulators. First, to realize constructive interference, all binary-phase pixels within a superpixel may contribute to the field output whereas binary-amplitude counterparts must discard the contributions of half their pixels. Hence, BiPE superpixels exhibit an intrinsically higher optical efficiency. Moreover, owing to the stronger combinatorics arising from these extra field contributions (see Supplementary Note 4), BiPE superpixels can access over 10 times more possible output fields than equally sized superpixels based on binary amplitude modulation. Furthermore, the binary phase control ability of each individual pixel in a BiPE superpixel reduces the magnitude of the phase gradient required at the PLM to π, rather than the range of 2π required by superpixels based on binary amplitude modulation. This reduced magnitude moves the modulated light closer to the center of the diffraction envelope, resulting in diffraction efficiency increases for BiPE-superpixel-based CFM of 17.2% (for $n =4$) to 35.0% (for $n =3$) over its binary-amplitude counterpart (see Supplementary Note 3).

Although BiPE superpixels do not use all of the PLM's available phase levels, several advantages arise in using the PLM as a binary phase SLM. First, BiPE superpixels are not influenced by the non-uniform distribution of phase levels so far intrinsic to actual PLMs (see Supplementary Note 1 and Supplementary Fig. S1e) and thus represent a utilization of PLMs that maintains chip-level interchangeability similar to that of DMDs. Recently, in response to the nonlinearity of PLM phase responses, a technique was demonstrated using a carefully chosen subset of available displacement states to emulate an approximately linear device response[31]. Regarded as an extreme case of this "forced linearization" approach, BiPE superpixels may be viewed as implementing the strategy minimizing the variability of modulation quality on device-specific characteristics. Moreover, while the restriction of a 4-bit PLM to 1-bit operation constitutes an under-utilization of the available degrees of freedom, it creates the opportunity for the design of future MEMS phase modulators. Specifically, the design of an intrinsically binary-mode PLM can be contemplated that, if using DMD-like fabrication upon a CMOS memory layer akin to current PLM development, could double the horizontal and vertical mirror resolution of the current multi-actuation PLM device by expanding each 16-state pixel into a 2×2 block of two-

state micromirrors. Since BiPE superpixels, akin to other superpixel-based methods, fundamentally achieve complex modulation through a sacrifice of the modulator's spatial resolution, such an increase of pixel count on a hypothetical PLM device would represent a complimentary development to the BiPE-superpixel technique, potentially leading to a doubling in the resolution of controllable points in the target plane.

The maximum modulation speed demonstrated in this work was limited by the native pattern refresh rate (1.44 kHz) of the deployed PLM. This constraint, imposed by the PLM driver electronics and firmware currently available from Texas Instruments, reflects the PLM's future intended market targeting color display applications involving the equal duration display of three 8-bit color RGB channels at an overall framerate of 60 Hz. However, reported actuation times of PLM micromirrors, as low as 50 µs, suggest the potential of BiPE-superpixel-based CFM at 20 kHz analogous to the performance of DMD-based methods[27]. In this way, improvements to driver electronics and firmware available for the control of PLMs stand to directly benefit CFM using BiPE superpixels in the future.

Although so far only demonstrated with offline computation, the pattern processing steps of BiPE-superpixel-based CFM could use various optimization strategies such as pre-computation and parallelization. Alternatively, more sophisticated algorithms designed to trade-off higher CFM quality and/or spatial bandwidth could be adapted for BiPE superpixels[40,41]. Our future work includes the development of such pattern generation algorithms that could be carried out rapidly across an array of superpixels using pre-computed lookup tables and/or multi-core computing hardware such as graphics processing units. This ability will propel the BiPE-superpixel approach for CFM applications demanding adaptive display and/or featuring lightweight computational resources.

AUTHOR CONTRIBUTIONS

P.K. designed the pattern generation algorithm, assisted in system development and construction, performed some experiments, and analyzed the data. J. Liu built the system, performed all experiments, and analyzed the data. J. Liang, Y.W., and L.G. initiated the project. J. Liang conceived the principle, contributed to experimental design, and supervised the project. P.K., J. Liu, and J. Liang drafted the manuscript. All authors wrote and revised the manuscript.

DATA AVAILABILITY

All data are available from the corresponding author upon reasonable request.

CONFLICT OF INTERESTS

The authors declare no competing interests.

REFERENCES

1. Cho, J. et al. Shaping lightwaves in time and frequency for optical fiber communication. *Nature Communications* **13**, 785 (2022).

2. Gong, L. et al. Optical orbital-angular-momentum-multiplexed data transmission under high scattering. *Light: Science & Applications* **8**, 27 (2019).

3. Pi, D. P., Liu, J. & Wang, Y. T. Review of computer-generated hologram algorithms for color dynamic holographic three-dimensional display. *Light: Science & Applications* **11**, 231 (2022).

4. Zhang, H., Cao, L. C. & Jin, G. F. Three-dimensional computer-generated hologram with Fourier domain segmentation. *Optics Express* **27**, 11689-11697 (2019).

5. Xu, X., Liu, H. L. & Wang, L. H. V. Time-reversed ultrasonically encoded optical focusing into scattering media. *Nature Photonics* **5**, 154-157 (2011).

6. Judkewitz, B. et al. Speckle-scale focusing in the diffusive regime with time reversal of variance-encoded light (TROVE). *Nature Photonics* **7**, 300-305 (2013).

7. Hampson, K. M. et al. Adaptive optics for high-resolution imaging. *Nature Reviews Methods Primers* **1**, 68 (2021).

8. Macintosh, B. et al. First light of the Gemini Planet Imager. *Proceedings of the National Academy of Sciences of the United States of America* **111**, 12661-12666 (2014).

9.   Liang, J. Y. et al. Homogeneous one-dimensional optical lattice generation using a digital micromirror device-based high-precision beam shaper. *Journal of Micro/Nanolithography*, *MEMS*, *and MOEMS* **11**, 023002 (2012).

10.   Chang, C. et al. High-brightness X-ray free-electron laser with an optical undulator by pulse shaping. *Optics Express* **21**, 32013-32018 (2013).

11.   Park, B. et al. Reflection‐mode switchable subwavelength Bessel‐beam and Gaussian‐beam photoacoustic microscopy in vivo. *Journal of Biophotonics* **12**, e201800215 (2019).

12.   Shi, J. H. et al. Bessel-beam Grueneisen relaxation photoacoustic microscopy with extended depth of field. *Journal of Biomedical Optics* **20**, 116002 (2015).

13.   Zhang, O. M. et al. Imaging the three-dimensional orientation and rotational mobility of fluorescent emitters using the Tri-spot point spread function. *Applied Physics Letters* **113**, 031103 (2018).

14.   Valliappan, N. et al. Accelerating eye movement research via accurate and affordable smartphone eye tracking. *Nature Communications* **11**, 4553 (2020).

15.   Chen, P. et al. Liquid-Crystal-Mediated Geometric Phase: From Transmissive to Broadband Reflective Planar Optics. *Advanced Materials* **32**, 1903665 (2020).

16.   Wei, B. Y. et al. Generating switchable and reconfigurable optical vortices via photopatterning of liquid crystals. *Advanced Materials* **26**, 1590-1595 (2014).

17.   Lazarev, G. et al. Beyond the display: phase-only liquid crystal on Silicon devices and their applications in photonics [Invited]. *Optics Express* **27**, 16206-16249 (2019).

18.   Yang, D. K. & Wu, S. T. Fundamentals of Liquid Crystal Devices. (Hoboken: John Wiley & Sons, Ltd., 2006).

19.   Madec, P. Y. Overview of deformable mirror technologies for adaptive optics and astronomy. Proceedings of SPIE 8447, Adaptive Optics Systems III. Amsterdam, Netherlands: SPIE, 2012, 844705.

20.   Dalimier, E. & Dainty, C. Comparative analysis of deformable mirrors for ocular adaptive optics. *Optics Express* **13**, 4275-4285 (2005).

21.   Stewart, J. B. et al. Design and development of a 331-segment tip–tilt–piston mirror array for space-based adaptive optics. *Sensors and Actuators A*: *Physical* **138**, 230-238 (2007).

22.   Hornbeck, L. J. Digital light processing for high-brightness high-resolution applications. Proceedings of SPIE 3013, Projection Displays III. San Jose, CA, United States: SPIE, 1997, 109320S.

23.   Lee, W. H. Binary synthetic holograms. *Applied Optics* **13**, 1677-1682 (1974).

24.   Lee, W. H. Computer-generated holograms: techniques and applications. *Progress in Optics* **16**, 119-232 (1978).

25.   Goorden, S. A., Bertolotti, J. & Mosk, A. P. Superpixel-based spatial amplitude and phase modulation using a digital micromirror device. *Optics Express* **22**, 17999-8009 (2014).

26.   Gutiérrez-Cuevas, R. & Popoff, S. M. Binary amplitude holograms for shaping complex light fields with digital micromirror devices. *Journal of Physics: Photonics* **6**, 045022 (2024).

27.   Bartlett, T. A., McDonald, B. C. & Hall, J. Adapting Texas instruments DLP technology to demonstrate a phase spatial light modulator. Proceedings of SPIE 10932, Emerging Digital Micromirror Device Based Systems and Applications XI. San Francisco, CA, United States: SPIE, 2019, 109320S.

28.   Oden, P. I. et al. Innovations with a massively paralleled, microelectromechanical systems (MEMS) toward piston-mode-based phase light modulator (PLM). Proceedings of SPIE 11294, Emerging Digital Micromirror Device Based Systems and Applications XII. San Francisco, CA, United States: SPIE, 2020, 112940G.

29.   Bartlett, T. A. et al. Recent advances in the development of the Texas Instruments phase-only microelectromechanical systems (MEMS) spatial light modulator. Proceedings of SPIE 11698, Emerging Digital Micromirror Device Based Systems and Applications XIII. SPIE, 2021, 116980O.

30.   Blanche, P. A. & Ketchum, R. S. Texas Instruments phase light modulator for holography. Proceedings of the OSA Imaging and Applied Optics Congress 2021, Digital Holography and Three-Dimensional Imaging. Washington, DC, United States: Optica Publishing Group, 2021, DW4B.3.

31.   Ketchum, R. S. & Blanche, P. -A. Diffraction efficiency characteristics for MEMS-based phase-only spatial light modulator with nonlinear phase distribution. *Photonics* **8**, 62 (2021).

32.   Khonina, S. N. et al. Bessel beam: significance and applications-a progressive review. *Micromachines* **11**, 997 (2020).

33.   Kennedy, S. A. et al. Creation of Laguerre-Gaussian laser modes using diffractive optics. *Physical Review A* **66**, 043801 (2002).

34.   Suchand Sandeep, C. S. et al. Bessel beams in ophthalmology: a review. *Micromachines* **14**, 1672 (2023).

35.   Grillo, V. et al. Generation and application of Bessel beams in electron microscopy. *Ultramicroscopy* **166**, 48-60 (2016).

36.   Vicidomini, G., Bianchini, P. & Diaspro, A. STED super-resolved microscopy. *Nature Methods* **15**, 173-182 (2018).

37.   Bustamante, C. J. et al. Optical tweezers in single-molecule biophysics. *Nature Reviews Methods Primers* **1**, 25 (2021).

38.   Paterson, L. et al. Controlled rotation of optically trapped microscopic particles. *Science* **292**, 912-914 (2001).

39.   Kovalev, A. A., Kotlyar, V. V. & Porfirev, A. P. Optical trapping and moving of microparticles by using asymmetrical Laguerre–Gaussian beams. *Optics Letters* **41**, 2426-2429 (2016).

40.   Jiao, S. et al. Complex-amplitude holographic projection with a digital micromirror device (DMD) and error diffusion algorithm. *IEEE Journal of Selected Topics in Quantum Electronics* **26**, 2800108 (2020).

41.   Yu, S. T. et al. Direct binary search method for high-resolution holographic image projection. *Optics Express* **30**, 26856 (2022).
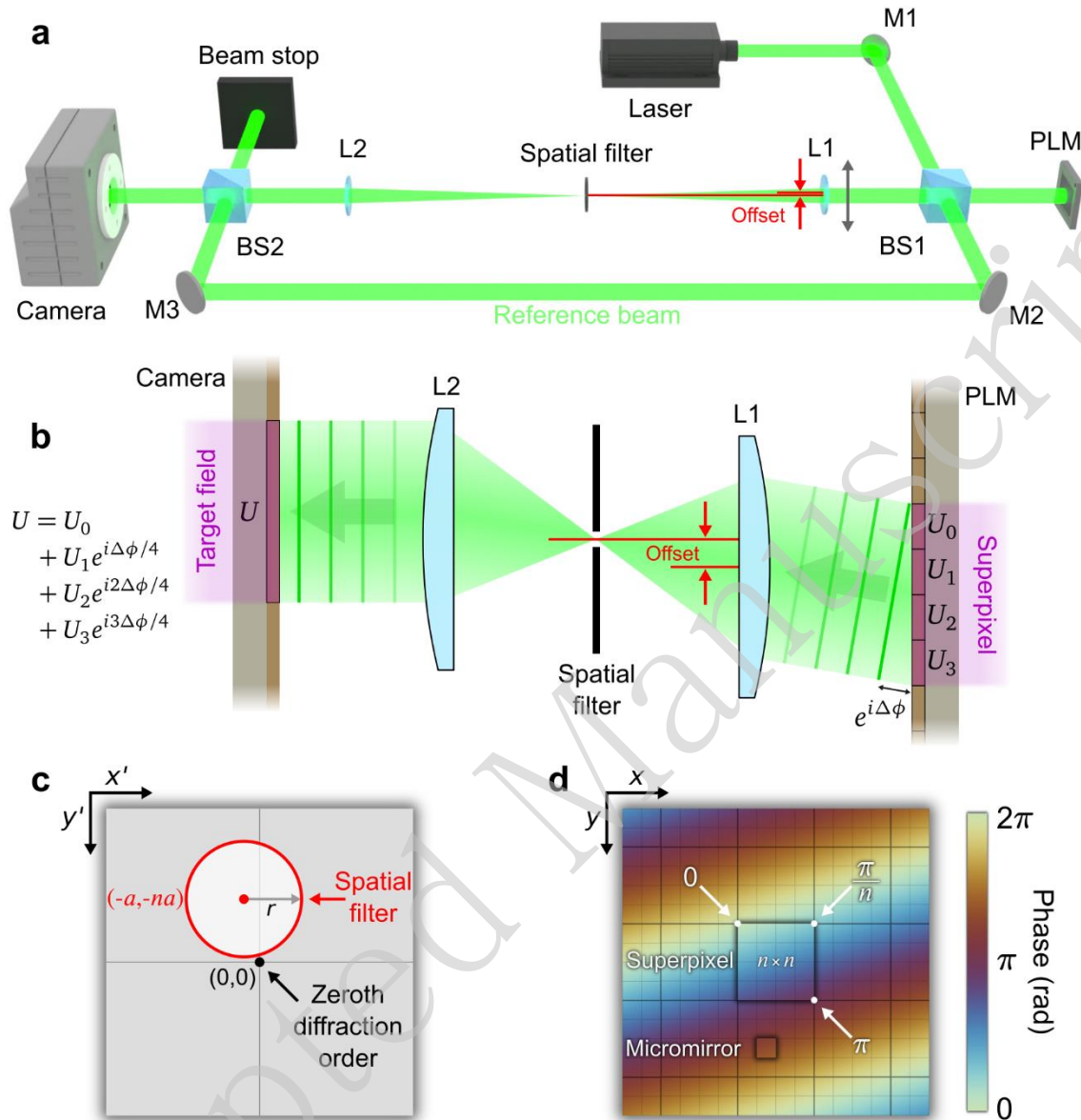
Fig. 1

Principle of complex field modulation (CFM) using binary phase-engraved (BiPE) superpixels. a System schematic. BS1 and BS2, beamsplitters; L1 and L2, lenses; M1–M3, mirrors; PLM, phase light modulator. **b** Side-profile illustration of a one-dimensional (1D) BiPE superpixel of size $n = 4$. **c** Illustration of the spatial filter showing the offset from the zeroth diffraction order of the PLM in units of $a = \frac{\lambda f}{2dn^2}$. **d** Illustration of the phase pre-factor created at the PLM surface, with boundary phase values and the footprints of superpixels and individual micromirrors highlighted.
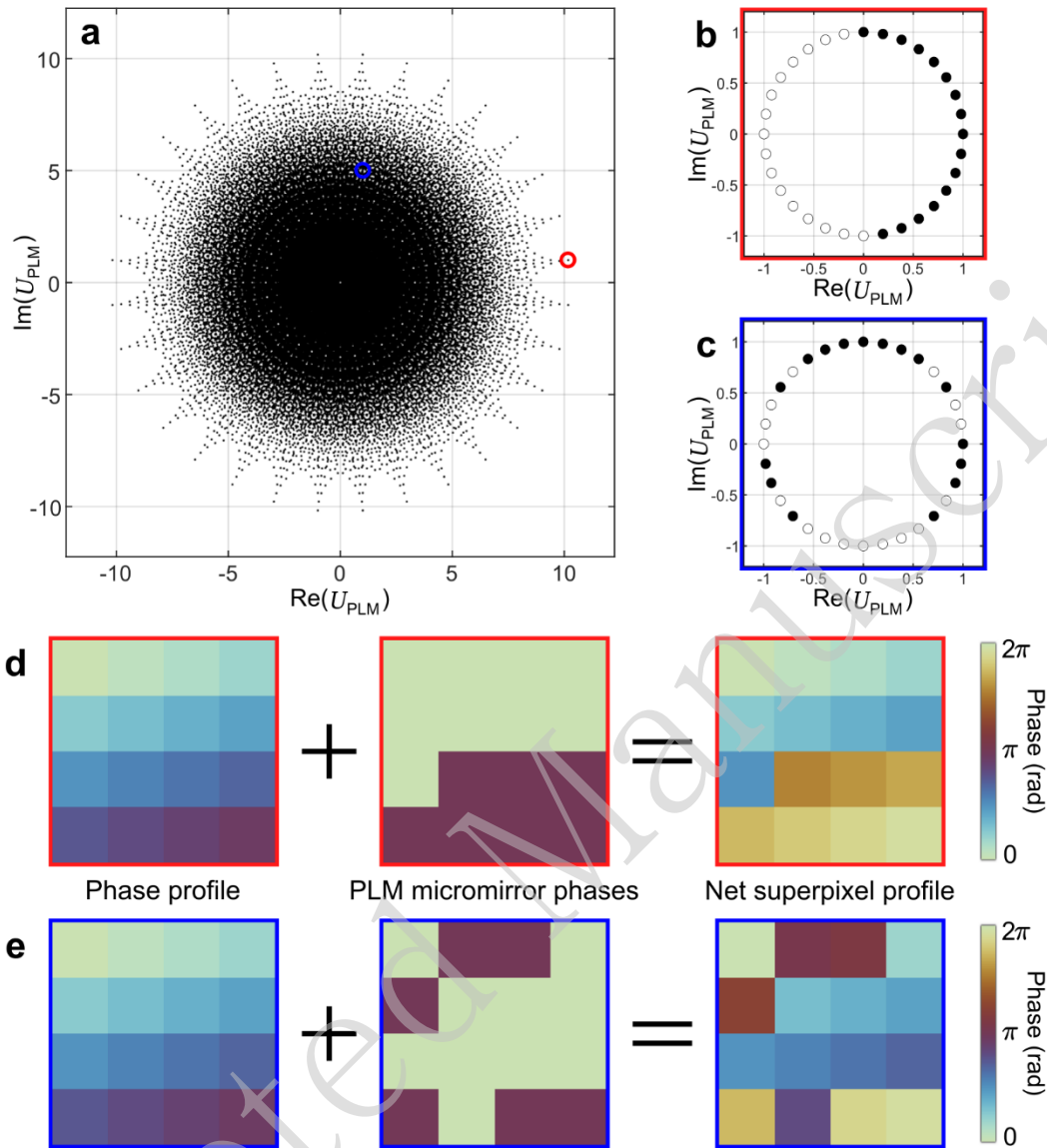
Fig. 2

Modulation capability using BiPE superpixels. a Gamut of 65,536 complex field values achievable by a 4×4 BiPE superpixel. **b** Complex plane phasor diagram of a representative BiPE superpixel whose produced complex field is marked by the red circle in (**a**). **c** As in (**b**), but for a different superpixel whose produced complex field is marked by the blue circle in (**a**). **d** Visualization of the creation of the phasor configuration shown in (**b**) via the contributions of the phase profile and phase contributions of individual PLM micromirrors. **e** As in (**d**), but corresponding to the phasor configuration shown in (**c**).
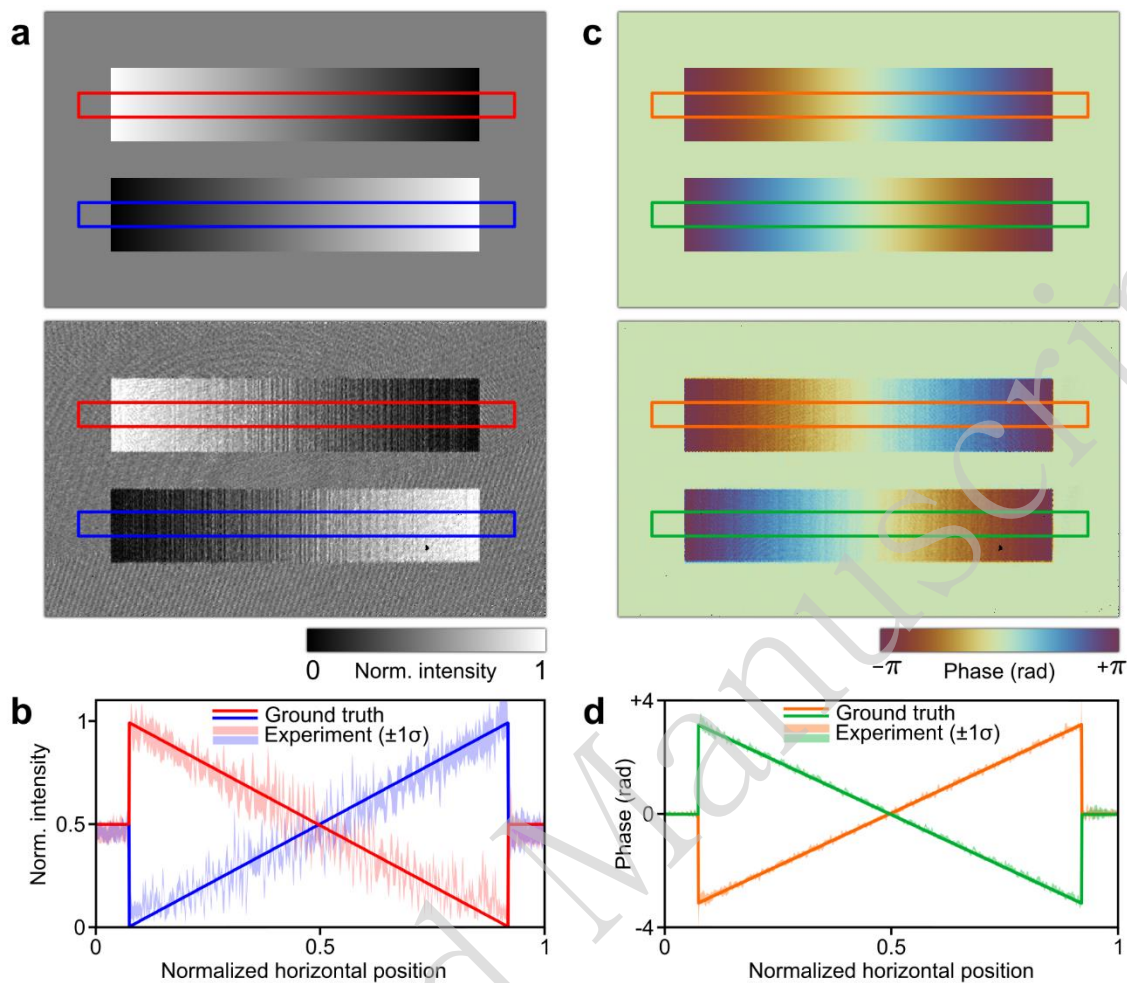
Fig. 3

Independent amplitude and phase field control using BiPE superpixels. a Ground truth (top)
and experimentally recorded (bottom) amplitude profiles of a double ramp. **b** Average amplitude
profiles of the blue and red boxed regions shown in (**a**). Variance band statistics are included for
the experimental data. **c** As in (**a**) but for a phase-encoded double ramp profile. **d** Average phase
profiles with included variance bands of the orange and green boxed regions shown in (**c**).
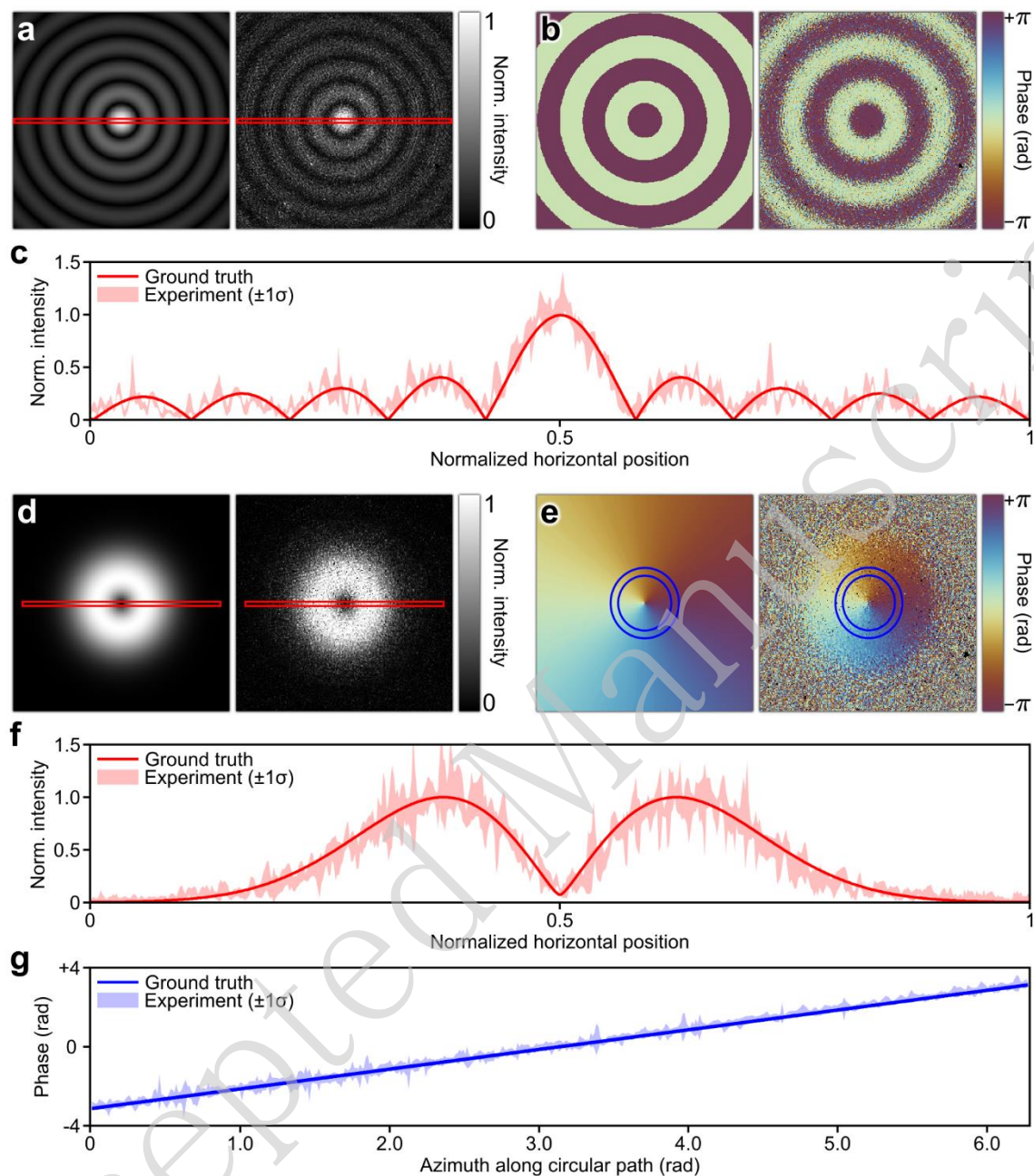
Fig. 4

Generation of complex optical fields using BiPE superpixels. a Ground truth (left) and experimentally recorded (right) field amplitude profiles for a Bessel beam. **b** As in (**a**) but for the phase profile of the Bessel beam. **c** Average amplitude profiles from the red-boxed regions shown in (**a**). Variance band statistics are included for the experimental data. **d** Ground truth (left) and experimentally recorded (right) field amplitude for the Laguerre-Gaussian donut beam. **e** As in (**d**) but for the phase profile of the Laguerre-Gaussian beam. **f** Comparison plot of amplitude profiles with variance bands from the red boxed regions shown in (**d**). **g** Average phase profiles plotted as a function of azimuthal angle with variance bands for the blue annular region shown in (**e**).
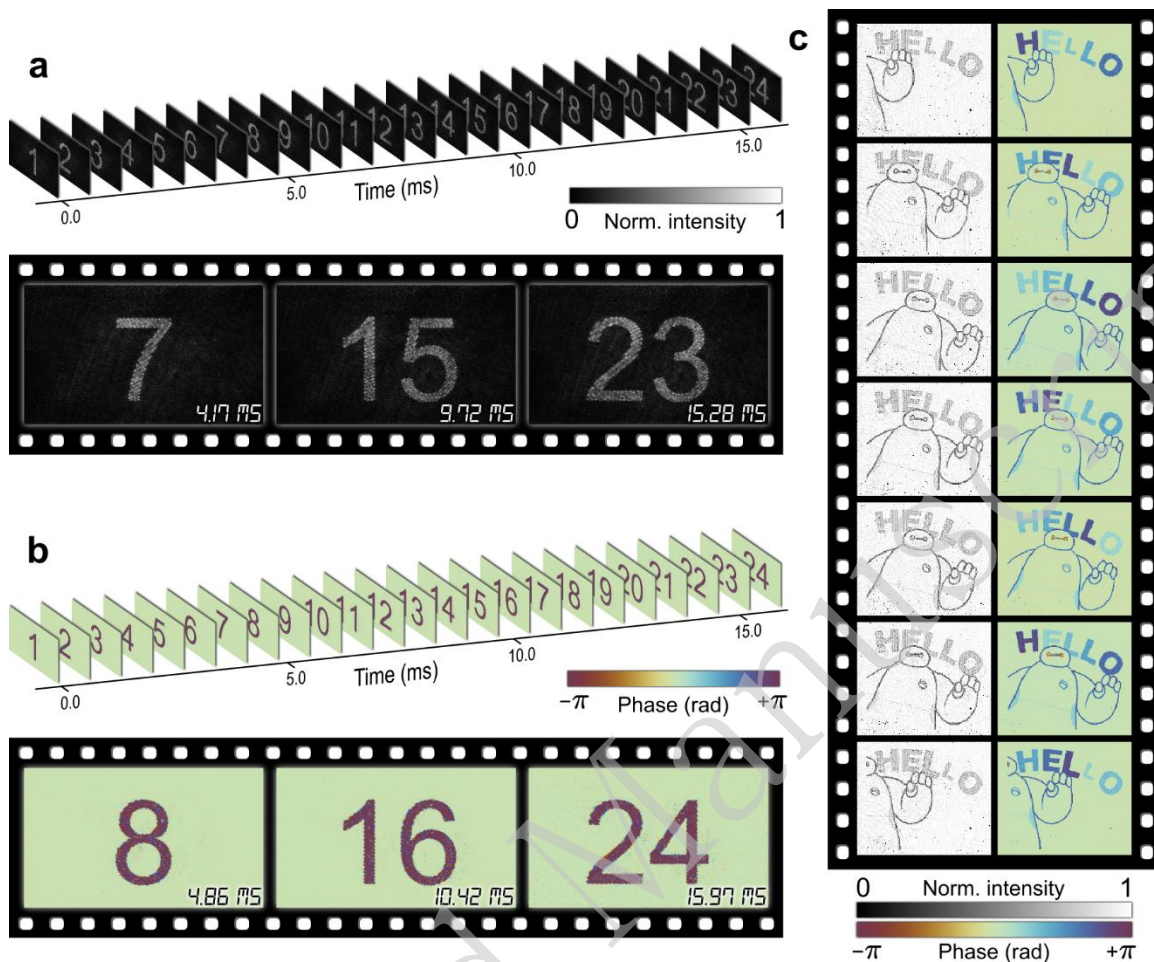
Fig. 5

Advanced display using BiPE-superpixel-based CFM. a Recovered amplitudes for a 24-frame sequence (top) depicting bright digits on a dark background displayed continuously at 1.44 kHz, with selected frames enlarged with timestamps (bottom). **b** As in (**a**) but for recovered phases for a sequence depicting the same digits as phase-only fields. **c** Recovered amplitudes (left) and phases (right) for selected frames from a complex field animation displayed at 60 Hz.
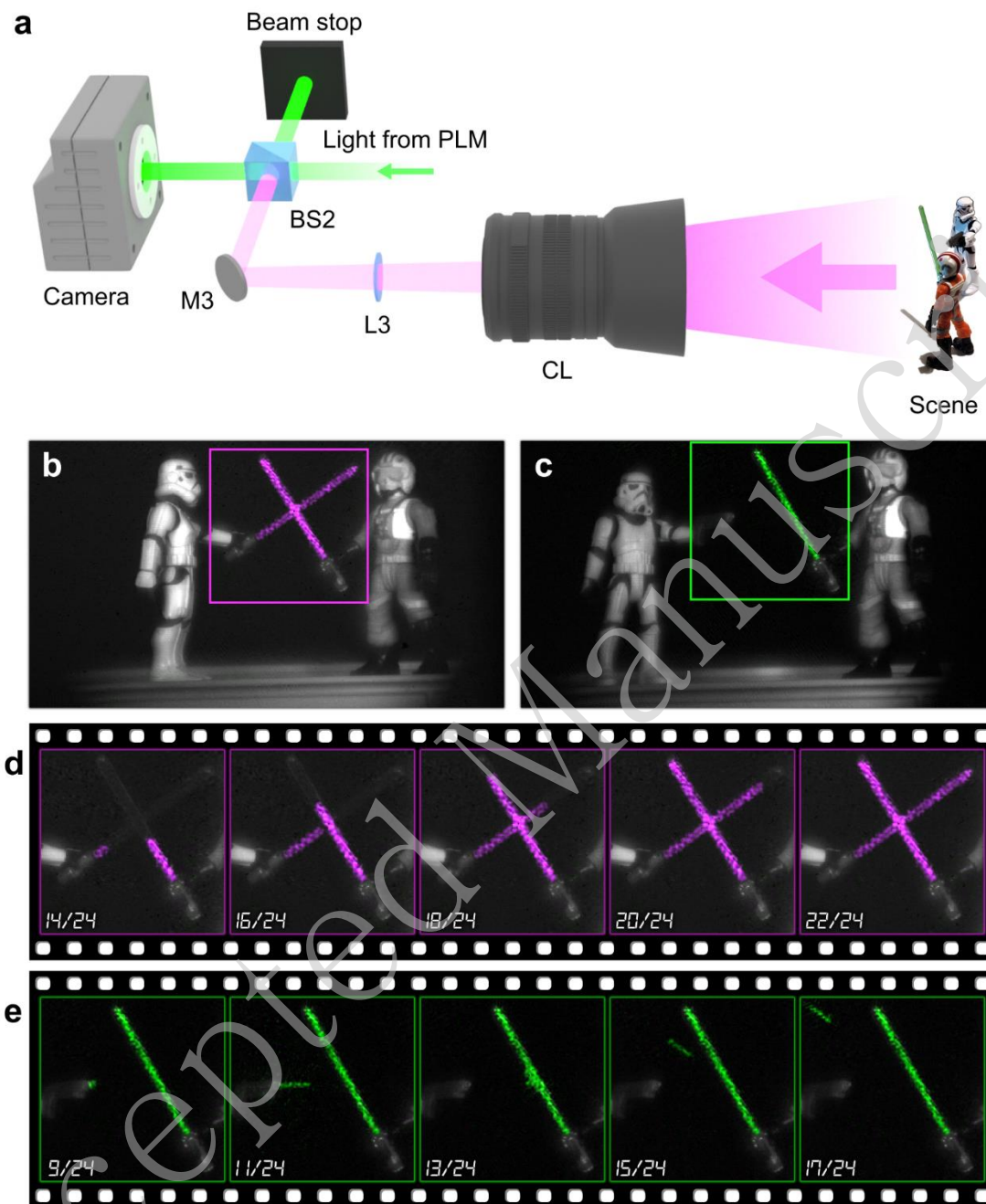
Fig. 6

Augmented reality (AR) display using BiPE-superpixel-based CFM. a Experiment schematic. CL, camera lens. **b, c** Scene overviews showing figurine poses and AR displayed by the PLM. **d** Sequence of selected animation frames from the AR scene in (**b**). **e** Sequence of selected animation frames from the AR scene in (**c**).